metals

MDPI

Article

A Solution to the Hot Cracking Problem and Anisotropic Mechanical Properties for Directed Energy Deposition FeCoNiCr Multi-Principal-Element Alloy

Liufei Huang [1,2], Rui Li [3], Yaoning Sun [2], Denggao Guan [3,*], Chuanhui Liang [1], Chunli Jiang [1], Jun Chen [1], Dou Wang [1] and Jinfeng Li [1,*]

[1] Institute of Materials, China Academy of Engineering Physics, Mianyang 621908, China
[2] School of Mechanical Engineering, Xinjiang University, Urumqi 830017, China
[3] College of Materials and Chemistry & Chemical Engineering, Chengdu University of Technology, Chengdu 610059, China
* Correspondence: gdg@cdut.edu.cn (D.G.); lijinfeng305@126.com (J.L.); Tel.: +86-028-84073628 (D.G.); +86-16659609259 (J.L.)

Abstract: In this paper, a laser-based directed energy deposition (DED) technique is used to fabricate FeCoNiCr and CrMnFeCoNi multi-principal-element alloys (MPEAs). Comparing the above samples, the FeCoNiCr samples with coarse columnar grains cracked, while the CrMnFeCoNi samples with equiaxed grain were crack-free. The strategy that removes cracks is to induce a columnar-grain-to-equiaxed-grain transition (CET) with Mn addition to offer more grain boundaries to withstand residual stress in the process of DED-fabricated FeCoNiCr and to help minimize hot cracking. Furthermore, the yield strength, tensile strength, and tensile ductility of the DED-fabricated CrMnFeCoNi obviously improved compared with the DED-fabricated CoCrFeNi and exhibited better isotropic mechanical properties. The present work provides a novel strategy to utilize CET for resisting crack propagation in the process DED-fabricated MPEAs and improvement in mechanical properties of MPEAs.

Keywords: multi-principal-element alloys; laser-based directed energy deposition; microstructure; tensile mechanical properties

check for updates

Citation: Huang, L.; Li, R.; Sun, Y.; Guan, D.; Liang, C.; Jiang, C.; Chen, J.; Wang, D.; Li, J. A Solution to the Hot Cracking Problem and Anisotropic Mechanical Properties for Directed Energy Deposition FeCoNiCr Multi-Principal-Element Alloy. *Metals* **2022**, *12*, 1581. https://doi.org/10.3390/met12101581

Academic Editor: Masahiro Fukumoto

Received: 8 August 2022
Accepted: 21 September 2022
Published: 23 September 2022

Publisher's Note: MDPI stays neutral with regard to jurisdictional claims in published maps and institutional affiliations.

Copyright: © 2022 by the authors. Licensee MDPI, Basel, Switzerland. This article is an open access article distributed under the terms and conditions of the Creative Commons Attribution (CC BY) license (https://creativecommons.org/licenses/by/4.0/).

1. Introduction

Multi-principal element alloys (MPEAs) have drawn widespread research interests due to their revolutionary idea for alloy design [1]. Usually, MPEAs are fundamentally different, with conventional alloys based on one or two dominant elements, because MPEAs contain equal or nearly equal quantities of four or more metallic elements, and prefer to form face-centered cubic (FCC) and/or body-centered cubic (BCC) solid solution phases rather than intermetallic phases [2]. This kind of unique microstructure provides MPEAs with excellent properties. One typical MPEA system is the CoCrFeNi and CoCrFeNi-based FCC alloys, which have attracted great interest due to increasing plasticity with decreasing temperature [3,4]. This alloy is a kind of excellent candidate material that is applied in low-temperature working environments, such as hulls, planes, low-temperature storage tanks, etc.

The fabrication of MPEAs mainly relies on conventional casting methods, such as vacuum arc-melting and then drop casting, which possesses significant disadvantages in terms of cost and efficiency [5,6]. With the development of additive manufacturing (AM), it provides a powerful and efficiency tool to obtain MPEAs with more homogeneous composition and complex geometry [7–10]. Columnar and equiaxed grains are the predominant microstructures for these AM-fabricated alloys [11–13]. However, the process of AM usually exhibits processing characteristics such as a high-temperature gradient

tending to form in the columnar grain along the molten pool boundaries in the deposited single-phase materials [14–17]. Generally, not only does a columnar grain structure induce the anisotropic properties of the materials but also its boundaries are sensitive locations for crack initiation [18,19].

It is reported that fine equiaxed microstructures can reduce the sensitivity to hot cracks and accommodate strains more easily [20,21]. For conventional alloys such as the Ti-6Al-4V alloy and the 316 L alloy, adjusting the energy input density in the process of AM is usually applied for facilitating the columnar-grain-to-equiaxed-grain transition (CET) to resist crack propagation and to improve the mechanical properties [22–26]. Recently, Xiang et al. [27] adopted this strategy and achieved an adjustment in the proportions of the columnar and equiaxed grains of DED-fabricated MPEAs. Furthermore, that paper presented the advantaged of DED technology compared with other AM methods, such as easily achieving CET transformation and promoting the mechanical properties. In order to expand the applications of CET in the MPEAs, we carried out a comparative study of the CoCrFeNi and CrMnFeCoNi that were manufactured by DED to provide insights into the correlation of CET and tensile mechanical properties with the compositions of MPEAs and to inspire tensile mechanical studies of other MPEAs.

2. Materials and Methods

The CoCrFeNi and CrMnFeCoNi samples were synthesized with the DED technique. The average sizes of alloyed CoCrFeNi and CrMnFeCoNi spherical powder were 120 μm via using a Microtrac S3500 laser particle size analyzer (Microtrac MRB, Montgomeryville, PA, USA). The chemical compositions of the pre-alloy in weight percent were measured by inductively coupled plasma mass spectrometry (ICP-OES) (Thermo Fisher Scientific, Waltham, MA, USA), as shown in Table 1. In the DED fabrication, the alloyed powder was sent through a coaxial nozzle into the laser molten pool on a 316 L steel substrate at an argon gas flow of 15–22 L/min and a feeding powder rate of 6–10 g/min. The manufacturing environment was under high-purity argon gas protection. Thin wall samples with lengths of ~80 mm and heights of ~40 mm were fabricated by laser multi-layer deposition. The optimal process parameters of DED-MPHAs were obtained via an orthogonal test: a laser power of 1200 W and a scanning speed of 400 mm/min. After each single laser scan, the laser head rose at 0.45 mm increments in height, keeping an 8 mm distance gap above the molten pool.

Table 1. Chemical compositions of the CoCrFeNi and CrMnFeCoNi MPEAs in weight percent measured by inductively coupled plasma mass spectrometry.

Element/wt.%	Co	Cr	Fe	Ni	Mn
CoCrFeNi	27.06	22.24	25.49	25.21	–
CrMnFeCoNi	22.58	17.92	19.94	20.28	19.28

The samples were disposed by spark erosion to study the microstructures of the plane, which consisted of the laser scanning direction (SD) and the deposition direction (DD). X-ray diffractometric with Cu-Kα radiation (XRD, D/max-RB, Rigaku, Japan), scanning electron microscopy (SEM, LEO1530) (LEO Electron Microscopes, Moorenweis, Germany) equipped with X-ray energy dispersive spectrometer (EDS) (Oxford Instruments, Abingdon, UK), and Zeiss Supra 35 instruments equipped with an Oxford Instruments electron backscatter diffraction (EBSD) system (Carl Zeiss AG, Jena, Germany) were applied to study the microstructure, fractography, and chemical composition distribution of the DED-fabricated samples. The thermal behaviors of the specimens were evaluated by differential scanning calorimetry (DSC, DSC-60, Shimadzu, Japan) at a heating rate of 20 K/min. The tensile mechanical properties of the samples were tested by an Instron 5982 static testing machine at a strain rate of 10^{-3} s^{-1}.

3. Results and Discussion

3.1. Microstructure Characteristics

Figure 1a exhibits some cracks that are parallel to the DD direction, observed on the surface of the DED-fabricated CoCrFeNi wall sample. For the CrMnFeCoNi wall samples in Figure 1b, there are surfaces without visible defects. Therefore, CrMnFeCoNi is better suited for DED technology than CoCrFeNi. The XRD spectrum of powders and corresponding DED-fabricated samples for the different alloy compositions are shown in Figure 1c. The XRD spectrum in Figure 1c shows the (111), (200), and (220) diffraction characteristic peaks of the face-centered cubic (FCC) single-phase solid solution for the four kinds of samples. For the CrMnFeCoNi composition, the peak intensity of the DED-fabricated sample and the corresponding powder maintained the same distribution, demonstrating no obvious preferential orientation. However, the peak intensity of the DED-fabricated CoCrFeNi sample had a different distribution from the corresponding powder. For the XRD spectrum of the DED-fabricated CoCrFeNi sample, the (200) peak intensity was stronger than the other peaks, indicating that crystal growth had a preferential orientation. Apparently, Mn addition exerted a significant effect on the crystal growth and grain distribution of the DED-fabricated CoCrFeNi samples. The DSC curves of both DED-fabricated samples are given in Figure 1d, where T_m corresponds to the beginning temperatures of the melting transitions observed in the DSC traces for the respective alloys. It is presented in Figure 1d that the T_m of CoCrFeNi is reduced from 1693 K to 1553 K after Mn addition. Furthermore, there is just one melting peak observed in the DSC traces for the two kinds of alloys, meaning that each alloy had a stable solid solution below T_m.

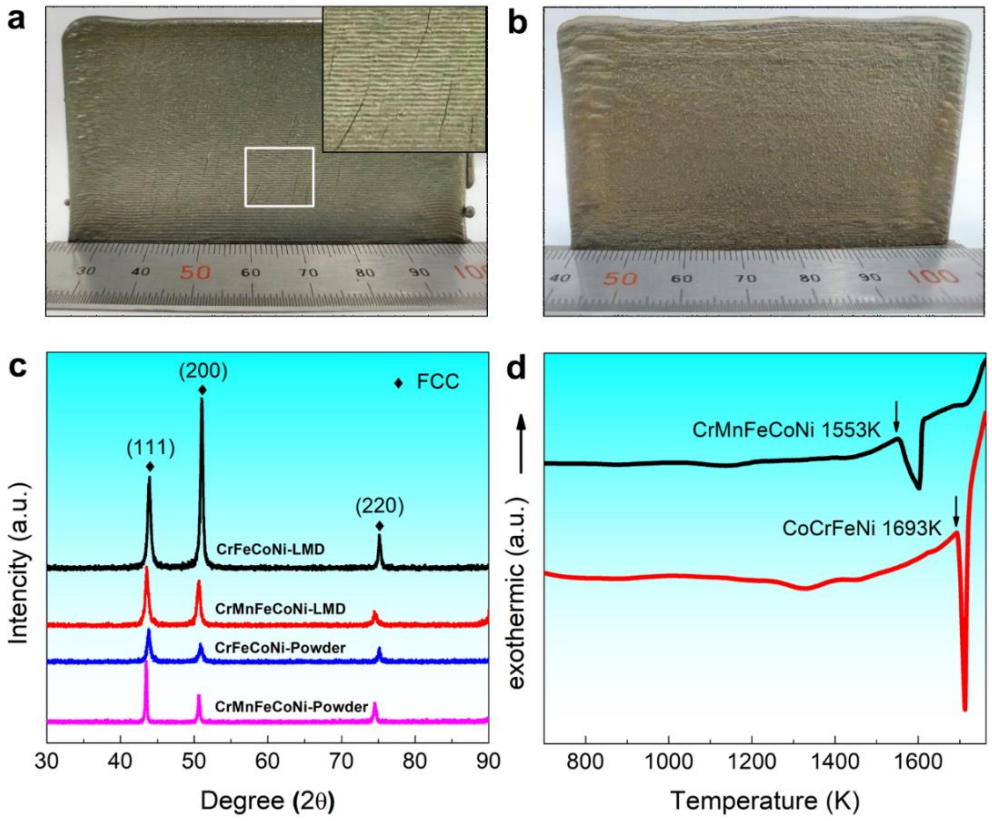

Figure 1. (**a**,**b**) DED-fabricated samples of CoCrFeNi and CrMnFeCoNi, respectively; (**c**) XRD spectrums and (**d**) DSC curves of the CoCrFeNi and CrMnFeCoNi MPEAs.

In order to further understand the function of Mn addition on the microstructure of DED-fabricated CoCrFeNi MPEA, the inverse pole figure (IPF) and pole figure (PF) of the samples obtained through EBSD analysis are presented in Figure 2. Figure 2a presents the

IPF map of the CoCrFeNi samples, with the columnar grain microstructure being ~1.2 mm in length and ~0.2 mm in width. Furthermore, the corresponding PF of CrFeCoNi shows that the orientation of most of the grains through the deposited direction are close to the <100> direction, exhibiting a strong texture, as displayed in Figure 2b. However, the IPF map in Figure 2c exhibits that the CrMnFeCoNi consists of the equiaxed grain with a mean size of ~150 μm. Figure 2d shows a random texture due to the occurrence of CET for DED-fabricated CrMnFeCoNi MPEAs.

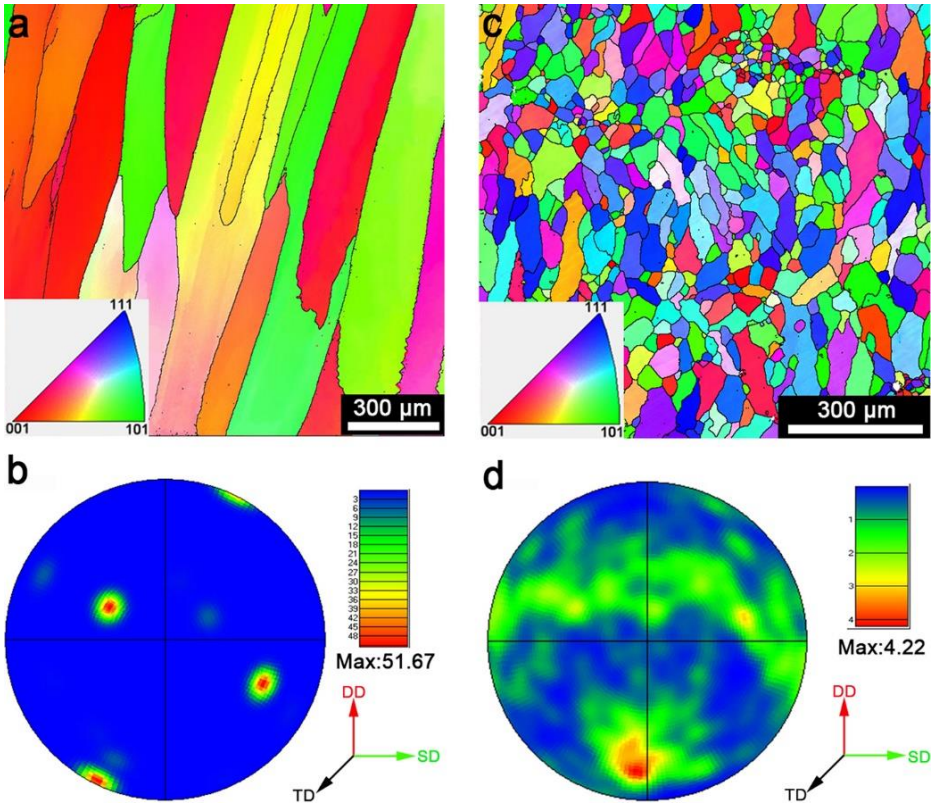

Figure 2. (**a**) The IPF coloring map and (**b**) PF maps of the DED-fabricated CoCrFeNi samples. (**c**) The IPF coloring map and (**d**) PF maps of the DED-fabricated CrMnFeCoNi samples.

The microstructure morphology is revealed to depend on the degree of undercooling. With the degree of undercooling increasing, the microstructure morphology will change from planar to cellular, to columnar dendritic, and then to equiaxed dendritic [28–30]. The degree of undercooling for a certain alloy depends on the solidification condition such as the temperature gradient (G) and the growth rate (R). For the solidification condition of an alloy, G is the highest at the bottom of the molten pool and R is the highest at the surface of the molten pool in DED process. The bottom region possesses the highest G/R value, where the columnar grains dominate the microstructure. Contrarily, the top region possesses the lowest G/R value, with the microstructure tending to be uniform equiaxed grains. The wall sample is formed by an overlap among adjacent one-layer layers [31]. The formation for a new layer is accompanied by a certain volume of the former layer to be melted, resulting in equiaxed grains that are only present at the top of the molten pool being melted. Therefore, the columnar grains at the bottom of former layer easily continue to grow epitaxially [12]. With Mn addition, the decreases in the T_m lead to more heat accumulation, which results in a decrease in the value of G/R over the entire region. The low G/R could promote the nucleation of equiaxed grains, thus forming an extensive equiaxed grain zone. Meanwhile, the epitaxial growth of columnar grains would be interrupted due to a new layer not being able to clear all of the equiaxed grains from the former layer, resulting in the formation of CET behavior for CrMnFeCoNi, as shown in Figure 2c.

Furthermore, the distribution of elements in each alloy has been comparatively examined. Figure 3a,b show that Co, Fe, Cr, and Ni are homogeneously distributed in CoCrFeNi with equiaxed grain microstructure samples. However, the CrMnFeCoNi with columnar grain microstructure samples exhibits dendrites enriched in Co, Fe, and Cr and interdendrimers enriched in Ni and Mn, as shown in Figure 3c,d. It is known that Mn and Ni have melting points of 1517 K and 1726 K, respectively, while Co, Cr, and Fe have melting points of 1768 K, 2130 K, and 1808 K, respectively. According to the report, the CrMnFeCoNi HEA can be described by a schematic phase diagram of the CrFeCo-MnNi system consisting of a liquid and a solid can be described by analogy with a completely miscible binary alloy [32]. Therefore, Mn and Ni, with lower melting points, are easily enriched in the interdendrites during the solidification of an alloy, as shown in Figure 3d.

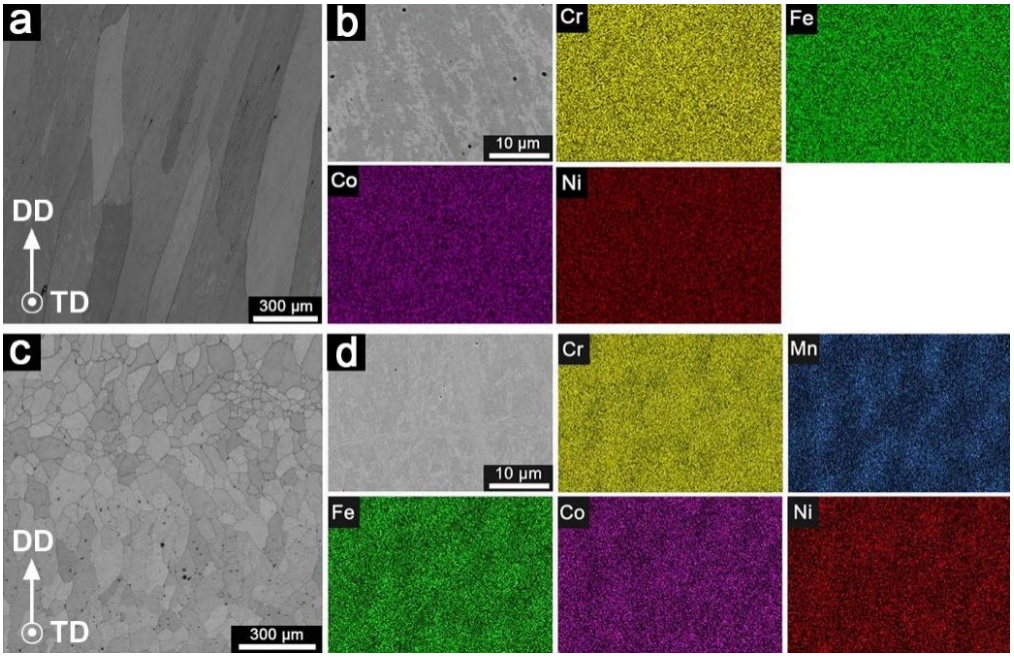

Figure 3. EDS maps of (**a**,**b**) CoCrFeNi and (**c**,**d**) CrMnFeCoNi samples prepared via DED.

3.2. Tensile Mechanical Properties

Figure 4a presents the tensile mechanical curves of CoCrFeNi and CrMnFeCoNi at room temperature, and the corresponded tensile mechanical properties are summarized in Table 2. Compared with the CoCrFeNi, the yield strength ($\sigma_{0.2}$), tensile strength (σ_{max}), and tensile ductility(ε) of CrMnFeCoNi along the DD and SD directions obviously improved. Furthermore, the CrMnFeCoNi samples in Figure 4a exhibit better isotropic mechanical properties than the CoCrFeNi samples.

To reveal the reasoning for the different tensile performances between the CoCrFeNi and CrMnFeCoNi samples, the corresponding cross-sectional SEM images of both fractured samples along the SD direction have been comparably studied in Figure 4b–e. Figure 4b shows that the CoCrFeNi sample displays the fracture of intergranular. Additionally, some elongated cracks were detected in the fracture of the CoCrFeNi sample in Figure 4b. Furthermore, cellular structure patterns, marked by the red arrow, have been observed on the enlarged image of the fracture in Figure 4c, exhibiting that intergranular micro hot cracks existed within the DED-fabricated CoCrFeNi samples. These intergranular hot cracks developed to elongated cracks under a load, leading to its property worsening and deviating. In Figure 4d, the fracture of the CrMnFeCoNi sample exhibits a necking behavior, demonstrating a ductile fracture mode under a tensile load. Furthermore, there is a dense population of dimples on the enlarged image of the fracture, as shown in Figure 4e, which also reflects the excellent plastic properties.

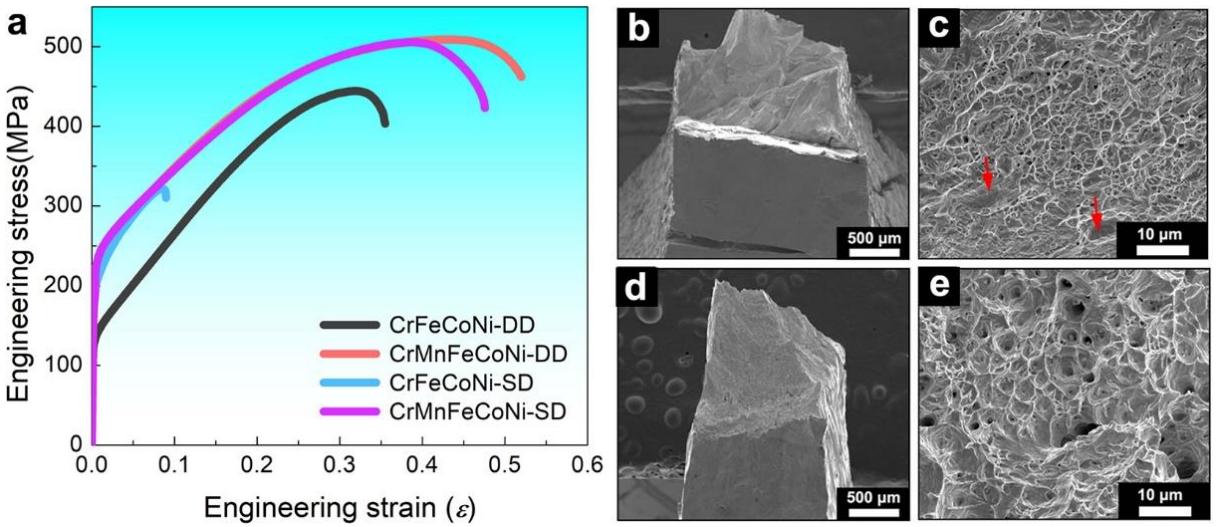

Figure 4. (**a**) The tensile curves of CoCrFeNi and CrMnFeCoNi along different direction; (**b**–**e**) the fracture surface of the CoCrFeNi (**b**,**c**) and CrMnFeCoNi (**d**,**e**) samples after tensile testing along the scanning direction.

Table 2. The tensile mechanical properties of CoCrFeNi and CrMnFeCoNi samples.

Materials	Direction	Yield Strength $\sigma_{0.2}$ (MPa)	Tensile Strength σ_{max} (MPa)
CrFeCoNi	DD	162 ± 8	444 ± 22
–	SD	241 ± 13	321 ± 18
CrMnFeCoNi	DD	255 ± 11	509 ± 26
–	SD	259 ± 9	505 ± 23

To conclude, the hot cracking problem and anisotropic mechanical properties for DED-fabricated FeCoNiCr MPEAs have been solved. There were limited residual liquids or/and semi-solids along the columnar grain boundaries at the last stage of solidification [29]. This is known as liquid feeding, in which unsolidified metals prefer to fill up open channels under the force of gravity/via capillary action. Cleavages, porosities, and other defects tend to be generated within the grain boundaries, when the channel of liquid feeding to mushy regions is hindered. Meanwhile, the tension force perpendicular to the grain boundary ascribed to residual stress is generated due to thermal shrinkage [18]. The large grains tend to form severe residual stress and easily experience pressures beyond the characteristic pressures at which hot cracking tends to start [33,34]. A CET behavior can refine the grain size to offer more grain boundaries to withstand the tension force and to help reduce hot cracking. Therefore, CrMnFeCoNi with equiaxed grains conquers the hot tearing issue for CoCrFeNi with columnar grains in DED processing, resulting in improvements in the mechanical properties.

4. Conclusions

In this paper, CoCrFeNi and CrMnFeCoNi MPEAs have been successfully fabricated with the DED technique. Additionally, the effect of Mn addition on the grain microstructure and mechanical properties of DED-fabricated CoCrFeNi were studied. The following can be concluded:

(1) With Mn addition, the microstructure of DED-fabricated CoCrFeNi transitioned from the columnar grain to the equiaxed grain.
(2) The hot cracking problem and the anisotropic mechanical properties have been solved for the DED-fabricated CoCrFeNi MPEAs with Mn addition.

(3) Compared with the CoCrFeNi, the yield strength, tensile strength, and tensile ductility of CrMnFeCoNi obviously improved and exhibited better isotropic mechanical properties.
(4) The CET induced by controlling the compositions has been applied to resist crack propagation and improvements in AM-fabricated MPEA mechanical properties.

Author Contributions: Conceptualization, J.L. and D.G.; methodology, L.H. and D.W.; software, R.L.; validation, L.H., R.L. and Y.S.; formal analysis, L.H.; investigation, C.L.; resources, C.J.; data curation, J.C.; writing—original draft preparation, L.H.; writing—review and editing, J.L.; visualization, L.H.; supervision, J.L.; project administration, R.L.; funding acquisition, J.L. All authors have read and agreed to the published version of the manuscript.

Funding: This research was funded by the CAEP Foundation (grant No. YZJJLX2019010 and grant No. CX2019020) and the National Natural Science Foundation of China (grant No. 52001288).

Data Availability Statement: The processed data required to reproduce these findings cannot be shared at this time as the data also form part of an ongoing study.

Conflicts of Interest: The authors declare no conflict of interest. We declare that we have no financial and personal relationships with other people or organizations that can inappropriately influence our work.

References

1. Li, Q.-J.; Sheng, H.; Ma, E. Strengthening in multi-principal element alloys with local-chemical-order roughened dislocation pathways. *Nat. Commun.* **2019**, *10*, 1–11. [CrossRef]
2. Long, Y.; Liang, X.; Su, K.; Peng, H.; Li, X. A fine-grained NbMoTaWVCr refractory high-entropy alloy with ultra-high strength: Microstructural evolution and mechanical properties. *J. Alloys Compd.* **2019**, *780*, 607–617. [CrossRef]
3. Gali, A.; George, E. Tensile properties of high- and medium-entropy alloys. *Intermetallics* **2013**, *39*, 74–78. [CrossRef]
4. Li, Z.; Zhao, S.; Ritchie, R.O.; Meyers, M.A. Mechanical properties of high-entropy alloys with emphasis on face-centered cubic alloys. *Prog. Mater. Sci.* **2019**, *102*, 296–345. [CrossRef]
5. Moghaddam, A.O.; Shaburova, N.A.; Samodurova, M.N.; Abdollahzadeh, A.; Trofimov, E.A. Additive manufacturing of high entropy alloys: A practical review. *J. Mater. Sci. Technol.* **2021**, *77*, 131–162. [CrossRef]
6. Chen, J.; Zhou, X.; Wang, W.; Liu, B.; Lv, Y.; Yang, W.; Xu, D.; Liu, Y. A review on fundamental of high entropy alloys with promising high–temperature properties. *J. Alloys Compd.* **2018**, *760*, 15–30. [CrossRef]
7. Chen, S.; Tong, Y.; Liaw, P.K. Additive Manufacturing of High-Entropy Alloys: A Review. *Entropy* **2018**, *20*, 937. [CrossRef]
8. Kim, J.; Wakai, A.; Moridi, A. Materials and manufacturing renaissance: Additive manufacturing of high-entropy alloys. *J. Mater. Res.* **2020**, *35*, 1963–1983. [CrossRef]
9. Amar, A.; Li, J.; Xiang, S.; Liu, X.; Zhou, Y.; Le, G.; Wang, X.; Qu, F.; Ma, S.; Dong, W.; et al. Additive manufacturing of high-strength CrMnFeCoNi-based High Entropy Alloys with TiC addition. *Intermetallics* **2019**, *109*, 162–166. [CrossRef]
10. Wang, Q.; Amar, A.; Jiang, C.; Luan, H.; Zhao, S.; Zhang, H.; Le, G.; Liu, X.; Wang, X.; Yang, X.; et al. CoCrFeNiMo0.2 high entropy alloy by laser melting deposition: Prospective material for low temperature and corrosion resistant applications. *Intermetallics* **2020**, *119*, 106727. [CrossRef]
11. Chadwick, A.F.; Voorhees, P.W. The development of grain structure during additive manufacturing. *Acta Mater.* **2021**, *211*, 116862. [CrossRef]
12. Tang, Y.T.; Panwisawas, C.; Ghoussoub, J.N.; Gong, Y.; Clark, J.W.G.; Nemeth, A.A.N.; McCartney, D.G.; Reed, R.C. Alloys-by-design: Application to new superalloys for additive manufacturing. *Acta Mater.* **2021**, *202*, 417–436. [CrossRef]
13. Tseng, J.C.; Huang, W.C.; Chang, W.; Jeromin, A.; Keller, T.F.; Shen, J.; Chuang, A.C.; Wang, C.C.; Lin, B.H.; Amalia, L.; et al. Deformations of Ti-6Al-4V additive-manufacturing-induced isotropic and anisotropic co-lumnar structures: In situ measurements and underlying mechanisms. *Addit. Manuf.* **2020**, *35*, 101322.
14. Aucott, L.; Dong, H.; Mirihanage, W.; Atwood, R.; Kidess, A.; Gao, S.; Wen, S.; Marsden, J.; Feng, S.; Tong, M.; et al. Revealing internal flow be-haviour in arc welding and additive manufacturing of metals. *Nat. Commun.* **2018**, *9*, 1–7. [CrossRef]
15. Kenel, C.; Casati, N.P.M.; Dunand, D.C. 3D ink-extrusion additive manufacturing of CoCrFeNi high-entropy alloy micro-lattices. *Nat. Commun.* **2019**, *10*, 1–8.
16. Pu, Z.; Du, D.; Wang, K.; Liu, G.; Zhang, D.; Wang, X.; Chang, B. Microstructure, phase transformation behavior and tensile superelasticity of NiTi shape memory alloys fabricated by the wire-based vacuum additive manufacturing. *Mater. Sci. Eng. A* **2021**, *812*, 141077. [CrossRef]
17. Zhang, C.; Li, Y.; Gao, M.; Zeng, X. Wire arc additive manufacturing of Al-6Mg alloy using variable polarity cold metal transfer arc as power source. *Mater. Sci. Eng. A* **2018**, *711*, 415–423. [CrossRef]
18. Kluczynski, J.; Sniezek, L.; Grzelak, K.; Torzewski, J.; Szachogluchowicz, I.; Wachowski, M.; Luszczek, J. Crack growth behavior of additively manufactured 316L steel-influence of build orientation and heat treatment. *Materials* **2020**, *13*, 3259. [CrossRef] [PubMed]

19. Lee, Y.; Kirka, M.; Ferguson, J.; Paquit, V. Correlations of cracking with scan strategy and build geometry in electron beam powder bed additive manufacturing. *Addit. Manuf.* **2020**, *32*, 101031. [CrossRef]
20. Liu, D.-R.; Wang, S.; Yan, W. Grain structure evolution in transition-mode melting in direct energy deposition. *Mater. Des.* **2020**, *194*, 108919. [CrossRef]
21. Wang, J.; Lin, X.; Wang, J.; Yang, H.; Zhou, Y.; Wang, C.; Li, Q.; Huang, W. Grain morphology evolution and texture characterization of wire and arc additive manufactured Ti-6Al-4V. *J. Alloys Compd.* **2018**, *768*, 97–113. [CrossRef]
22. Bermingham, M.; St John, D.; Krynen, J.; Tedman-Jones, S.; Dargusch, M. Promoting the columnar to equiaxed transition and grain refinement of titanium alloys during additive manufacturing. *Acta Mater.* **2019**, *168*, 261–274. [CrossRef]
23. Liu, P.; Wang, Z.; Xiao, Y.; Horstemeyer, M.F.; Cui, X.; Chen, L. Insight into the mechanisms of columnar to equiaxed grain transition during metallic additive manufacturing. *Addit. Manuf.* **2019**, *26*, 22–29. [CrossRef]
24. Tedman-Jones, S.; McDonald, S.; Bermingham, M.; StJohn, D.; Dargusch, M. A new approach to nuclei identification and grain refinement in titanium alloys. *J. Alloys Compd.* **2019**, *794*, 268–284. [CrossRef]
25. Wu, Y.; Zhang, S.; Cheng, X.; Wang, H. Investigation on solid-state phase transformation in a Ti-47Al-2Cr-2V alloy due to thermal cycling during laser additive manufacturing process. *J. Alloys Compd.* **2019**, *799*, 325–333. [CrossRef]
26. Zhou, K.; Li, J.; Wu, Q.; Zhang, Z.; Wang, Z.; Wang, J. Remelting induced fully-equiaxed microstructures with anomalous eutectics in the additive manufactured Ni32Co30Cr10Fe10Al18 eutectic high-entropy alloy. *Scr. Mater.* **2021**, *201*, 113952. [CrossRef]
27. Xiang, S.; Li, J.; Luan, H.; Amar, A.; Lu, S.; Li, K.; Zhang, L.; Liu, X.; Le, G.; Wang, X.; et al. Effects of process parameters on microstructures and tensile properties of laser melting deposited CrMnFeCoNi high entropy alloys. *Mater. Sci. Eng. A* **2019**, *743*, 412–417. [CrossRef]
28. Basak, A.; Das, S. Epitaxy and Microstructure Evolution in Metal Additive Manufacturing. *Annu. Rev. Mater. Sci.* **2016**, *46*, 125–149. [CrossRef]
29. Grong, O.; Shercliff, H. Microstructural modelling in metals processing. *Prog. Mater. Sci.* **2002**, *47*, 163–282. [CrossRef]
30. Zhang, H.; Pan, Y.; He, Y.-Z.; Wu, J.; Yue, T.M.; Guo, S. Application Prospects and Microstructural Features in Laser-Induced Rapidly Solidified High-Entropy Alloys. *JOM* **2014**, *66*, 2057–2066. [CrossRef]
31. Han, Q.; Gu, Y.; Setchi, R.; Lacan, F.; Johnston, R.; Evans, S.L.; Yang, S. Additive manufacturing of high-strength crack-free Ni-based Hastelloy X superalloy. *Addit. Manuf.* **2019**, *30*, 100919. [CrossRef]
32. Laurent-Brocq, M.; Akhatova, A.; Perrière, L.; Chebini, S.; Sauvage, X.; Leroy, E.; Champion, Y. Insights into the phase diagram of the CrMnFeCoNi high entropy alloy. *Acta Mater.* **2015**, *88*, 355–365. [CrossRef]
33. DebRoy, T.; Wei, H.L.; Zuback, J.S.; Mukherjee, T.; Elmer, J.W.; Milewski, J.O.; Beese, A.M.; Wilson-Heid, A.; De, A.; Zhang, W. Additive manufacturing of metallic components—Process, structure and properties. *Prog. Mater. Sci.* **2018**, *92*, 112–224. [CrossRef]
34. Yakout, M.; Elbestawi, M.; Veldhuis, S.C. Density and mechanical properties in selective laser melting of Invar 36 and stainless steel 316L. *J. Mater. Process. Technol.* **2019**, *266*, 397–420. [CrossRef]